Numerical evolutions of a black hole-neutron star system in full general relativity: Head-on collision

Frank Löffler

SISSA, International School for Advanced Studies and INFN, Via Beirut 2, 34014 Trieste, Italy and Max-Planck-Institut für Gravitationsphysik, Albert-Einstein-Institut, 14476 Potsdam, Germany

Luciano Rezzolla

Max-Planck-Institut für Gravitationsphysik, Albert-Einstein-Institut, 14476 Potsdam, Germany, SISSA, International School for Advanced Studies and INFN, Via Beirut 2, 34014 Trieste, Italy and Department of Physics, Louisiana State University, Baton Rouge, Louisiana 70803 USA

Marcus Ansorg

Max-Planck-Institut für Gravitationsphysik, Albert-Einstein-Institut, 14476 Golm, Germany

(Received 23 June 2006; published 14 November 2006)

We present the first simulations in full general relativity of the head-on collision between a neutron star and a black hole of comparable mass. These simulations are performed through the solution of the Einstein equations combined with an accurate solution of the relativistic hydrodynamics equations via high-resolution shock-capturing techniques. The initial data is obtained by following the York-Lichnerowicz conformal decomposition with the assumption of time symmetry. Unlike other relativistic studies of such systems, no limitation is set for the mass ratio between the black hole and the neutron star, nor on the position of the black hole, whose apparent horizon is entirely contained within the computational domain. The latter extends over $\sim 400M$ and is covered with six levels of fixed mesh refinement. Concentrating on a prototypical binary system with mass ratio ~ 6, we find that although a tidal deformation is evident the neutron star is accreted promptly and entirely into the black hole. While the collision is completed before $\sim 300M$, the evolution is carried over up to $\sim 1700M$, thus providing time for the extraction of the gravitational-wave signal produced and allowing for a first estimate of the radiative efficiency of processes of this type.

DOI: 10.1103/PhysRevD.74.104018 PACS numbers: 04.25.Dm, 04.30.Db, 04.70.Bw, 97.60.Jd

I. INTRODUCTION

Binary systems of compact bodies are believed to be among the major sources of gravitational waves, which could be detected with the newly built gravitational wave detectors. These compact objects can be black holes or very compact stars, like neutron stars. There is strong evidence that objects like neutron stars or black holes do exist [1] and even collide [2,3] in our universe. Amongst the astrophysical phenomena that are the best candidates for producing detectable wave signals for the Earth-based detectors, those including highly relativistic matter near black holes stand out. Black hole–neutron star binaries are believed to be as likely to be observed as binary neutron star mergers (see, for instance, [3]), with expected event rates of one per year in a sphere of about 70 Mpc radius [3] and an expected detection rate of more than one event per year [1] (for LIGO II). Gravitational-wave signals from binary neutron star and mixed binary systems in close orbit are expected to give information about the neutron star structure and equation of state (EOS) [1,4]. However calculating these gravitational waves is far too difficult to be done analytically, and numerical investigations are the only possible avenue in the final stages of the evolution, when nonlinear effects and finite-size contributions from the compact star need to be modeled accurately. The importance of such an accurate modeling, however, is that the analysis of the gravitational-wave signal could be used to obtain important information about the equation of state governing the matter of the compact star [5].

Mixed binaries are also interesting for a number of other reasons, e.g. they could be a source of short gamma-ray bursts (e.g. [6,7]), that typically last for about a fraction of a second [8]. Previous studies of the dynamics of mixed binary systems in Newtonian gravity and carried out either analytically [9], or through numerical simulations [10,11], suggest that a stable or repeated, but in any case long-lasting, mass transfer from the neutron star to the black hole is to be expected. However that might be different in general relativity [12], which is required in the presence of black holes. Considerable effort has gone into modeling systems of binaries containing either two black holes (e.g. [13–15] and references therein) or two neutron stars (e.g. [16,17] and references therein).

Research on *mixed* binary systems has traditionally been performed using Newtonian gravity. In particular, together with some analytical work on stable mass transfer from a neutron star to a black hole [9], numerical simulations have been carried out using smooth particle hydrodynamics (SPH) techniques and with either soft [10] or stiff [11]

equations of state. All of this bulk of work suggests that, depending on the mass ratio, at least part of the neutron star should be tidally disrupted before the merger. These approaches have also provided the first estimates of the gravitational-wave emission during the inspiral and merger by making use of the Newtonian quadrupole approximation [10,11] and indicating that the process has in general an efficiency of $\approx 0.7\%$. Shortly after, simulations by Janka *et al.* [18] included a realistic EOS and showed good agreement with this estimate.

More recently these studies have been improved with either the use of relativistic corrections to the Newtonian gravity in terms of pseudo-Newtonian potentials [19] or in general relativity but within a ''quasistationary'' approximation [20]. The latter assumes that the evolution of the binary system can be modeled through a sequence of quasistationary spacetimes, solutions of the Einstein equations. This is clearly an approximation but a very good one especially in those stages of the evolution of the system when the inspiral time scale is much longer than the orbital or the one associated to a dynamical instability.

However, as the separation between the two compact objects decreases, this approximation becomes less accurate and eventually breaks [21,22], forcing the use of fully dynamical simulations. A first step in this direction within a relativistic context has been made recently within the characteristic formulation of Einstein equations [23]. In this approach, it was shown that the initial spurious gravitational waves signal resulting from the approximations in the calculation of the initial data are rapidly radiated away and the binary system relaxes to a quasiequilibrium state with an approximate orbital motion of the star which has been followed only for a small fraction of an orbit.

A second step towards a more accurate description of the dynamics of a mixed binary system has been made by Faber *et al.* [24]. Taking as initial data the one computed in Ref. [20], Faber *et al.* have studied the final dynamics of the binary system using SPH techniques for the hydrodynamics and a conformally flat approximation to the Einstein equations. In these calculations the black hole is only included as a background metric in addition to the one of the neutron star and it is not included in the computational domain, thus limiting the investigation to rather large black hole-to-neutron star mass ratios. Overall, the results found indicate that rather generically, an accretion disc can be formed from the tidal disruption of the compact star and that this could, although short-lived, provide energy to power a gamma-ray burst. As an extension to the results presented in Ref. [24], Taniguchi *et al.* have considered the evolution of the system in the case in which the binary is irrotational [25], and found that the effect of the spin of the neutron star has only a minor effect on the location of the tidal break-up which plays an important role in the form of the gravitational waves produced. Sopuerta *et al.* took another approach [26] to the full problem. Here, the spacetime is treated in full general relativity, however, the hydrodynamics of the neutron star is frozen. This is a good approximation if the dynamical time scales related with the deformation of the neutron star are much bigger than the orbital time scales and also aims at large black hole-to-neutron star mass ratios.

While important first steps in the study of the dynamics of mixed binary systems in general relativity, the analysis carried out in Refs. [23–26] was not able to investigate binaries with comparable mass. This regime is far more demanding from a computational point of view as it requires the solution of the full Einstein equations, of accurate hydrodynamical techniques and, most importantly, the direct inclusion of the black hole's apparent horizon within the computational domain. In this context, the expectation is that the merger is prompt in most cases [12] with the formation of an accretion disc being very unlikely. This is expected to be the result of the intense angular-momentum loss due to gravitational radiation, which causes a direct merger rather than a slower and extended mass transfer.

Clearly, fully numerical calculations are needed to confirm this expectation and in this spirit we here consider the first simulations in full general relativity of the head-on collision between a neutron star and a black hole of comparable mass. We solve the Einstein equations combined with an accurate solution of the relativistic hydrodynamics equations via high-resolution shock-capturing (HRSC) techniques. The initial data is obtained by following the York-Lichnerowicz conformal decomposition with the assumption of time symmetry, using a spectral solver on one, compactified domain. Unlike the previously mentioned relativistic studies of such systems, no limitation is set for the mass ratio between the black hole and the neutron star, nor on the position of the black hole, whose apparent horizon is entirely contained within the computational domain. The latter extends over $\sim 400M$ and is covered with six levels of fixed mesh refinements. We concentrate on an example of a binary system with mass ratio ~ 6, and find that although a tidal deformation is evident the neutron star is accreted promptly and entirely into the black hole. The collision is completed before a time of $\sim 300M$, but we are able to obtain an evolution up to $\sim 1700M$, which provides enough time for the extraction of the gravitational-wave signal produced and allows for a first estimate of the radiative efficiency of processes of this type.

This paper is organized as follows: Sec. II describes the formulation used for the Einstein and hydrodynamics equations. The construction and testing of initial data for the mixed binary system is presented in Sec. III. Section IV is devoted to discussions about improved gauges and the use of dissipation together with excision, as well as the study of the dynamics of the merger, which depends on these techniques. Gravitational waves are one of the main motivations for this study, and in Sec. V we show the first

waveform obtained in a simulation in full general relativity of a head-on collision of a mixed binary of comparable mass and give an order-of-magnitude estimate of the energy emitted in gravitational waves. Finally, we conclude and outline our future plans in Sec. VI.

Throughout this paper Greek indices run from 0 to 3 indicating the four dimensions of spacetime and 0 referring to the direction of time. Unless otherwise stated, Latin indices run from 1 to 3. In all formulas indices occurring twice are to be summed over the possible range for that index. Unless stated otherwise, we adopt the convention of units in which $c = G = M_\odot = 1$. Where we measure times and lengths in units of M, we define $M \equiv M_\odot$.

II. BASIC EQUATIONS AND THEIR IMPLEMENTATION

The `Whisky` code solves the general relativistic hydrodynamics equations on a 3D numerical grid with Cartesian coordinates [27,28]. The code has been constructed within the framework of the `Cactus` Computational Toolkit, developed at the Albert Einstein Institute (Golm) and at the Louisiana State University (Baton Rouge). While the `Cactus` code provides at each time step a solution of the Einstein equations [29]

$$G_{\mu\nu} = 8\pi T_{\mu\nu}, \tag{1}$$

where $G_{\mu\nu}$ is the Einstein tensor and $T_{\mu\nu}$ is the stress-energy tensor, the `Whisky` code provides the time evolution of the hydrodynamics equations, expressed through the conservation equations for the stress-energy tensor $T^{\mu\nu}$ and for the matter current density J^μ

$$\nabla_\mu T^{\mu\nu} = 0, \qquad \nabla_\mu J^\mu = 0. \tag{2}$$

Hereafter we will consider the dynamics of perfect fluids described by a stress-energy tensor

$$T^{\mu\nu} = \rho h u^\mu u^\nu + p g^{\mu\nu}, \tag{3}$$

where $h \equiv 1 + \epsilon + p/\rho$ is the specific enthalpy, while p, ρ and ϵ indicate the pressure, the rest-mass density and the internal energy density, respectively. Furthermore, we will assume the fluid to obey an "ideal fluid" (Γ-law) equation of state

$$p = (\Gamma - 1)\rho\epsilon, \tag{4}$$

which, for $\Gamma = 2$, provides a reasonably good approximation for a stiff equation of state.

In what follows we briefly discuss how both the right and the left-hand side of Eq. (1) are computed within the coupled `Cactus/Whisky` codes.

A. Evolution of the field equations

We here give only a brief overview of the system of equations for the evolution of the field equations, but refer the reader to [29] for more details. Many different formulations of the equations have been proposed throughout the years, starting with the ADM formulation in 1962 [30]. As mentioned in the Introduction, we use the conformal traceless formulation [31], which is based on the ADM construction and has been further developed in [32].

Details of our particular implementation are extensively described in [29,33] and will not be repeated here. We only recall that this formulation makes use of a conformal decomposition of the three-metric, $\tilde{\gamma}_{ij} = e^{-4\phi}\gamma_{ij}$, and the trace-free part of the extrinsic curvature, $A_{ij} = K_{ij} - \gamma_{ij}K/3$, with the conformal factor ϕ chosen to satisfy $e^{4\phi} = \gamma^{1/3}$, where γ is the determinant of the spatial three-metric γ_{ij}. In this formulation, in addition to the evolution equations for the conformal three-metric $\tilde{\gamma}_{ij}$ and for the conformal traceless extrinsic curvature $\tilde{A}_{ij}$, there are evolution equations for the conformal factor ϕ, for the trace of the extrinsic curvature K and for the "conformal connection functions" $\tilde{\Gamma}^i \equiv \tilde{\gamma}^{ij}_{,j}$. We note that although the final mixed, first-order in time and second-order in space, evolution system for ϕ, K, $\tilde{\gamma}_{ij}$, $\tilde{A}_{ij}$, $\tilde{\Gamma}^i$ is not in any immediate sense hyperbolic, there is evidence showing that the formulation is at least equivalent to a hyperbolic system (e.g. [34,35]).

Standard gauge choices

The code is designed to handle arbitrary shift and lapse conditions, which can be chosen as appropriate for a given spacetime simulation. More information about the possible families of spacetime slicings which have been tested and used with the present code can be found in [29,36]. Here, we limit ourselves to recalling details about the specific foliations used in the present evolutions. In particular, we have used hyperbolic K-driver slicing conditions of the form

$$(\partial_t - \beta^i\partial_i)\alpha = -f(\alpha)\alpha^2(K - K_0), \tag{5}$$

with $f(\alpha) > 0$ and $K_0 \equiv K(t = 0)$. This is a generalization of many well-known slicing conditions. For example, setting $f = 1$ we recover the "harmonic" slicing condition, while, by setting $f = q/\alpha$, with q an integer, we recover the generalized "1 + log" slicing condition [37]. In particular, all of the simulations discussed in this paper are done using condition (5) with $f = 2/\alpha$. This choice has been made mostly because of its computational efficiency, but we are aware that "gauge pathologies" could develop with the "1 + log" slicings (see e.g. [38]).

As for the spatial gauge, we use one of the "Gamma-driver" shift conditions proposed in [36], that essentially act so as to drive the $\tilde{\Gamma}^i$ to be constant. More specifically, all of the results reported here have been obtained using a (modified) hyperbolic Gamma-driver condition,

$$\partial_t^2\beta^i = F\partial_t\tilde{\Gamma}^i - \eta\partial_t\beta^i, \tag{6}$$

where F and η are, in general, positive functions of space

and time (We typically choose $F = 3/4$ and $\eta = 3$ and do not vary them in time.) For the hyperbolic Gamma-driver conditions it is crucial to add a dissipation term with coefficient η to avoid strong oscillations in the shift. Experience has shown that by tuning the value of this dissipation coefficient it is possible to almost freeze the evolution of the system at late times. As mentioned in [28], we here recall that the ''Gamma-driver'' shift conditions are similar to the ''Gamma-freezing'' condition $\partial_t \tilde{\Gamma}^k = 0$, which, in turn, is closely related to the well-known minimal distortion shift condition [39]. The differences between these two conditions involve the Christoffel symbols and are basically due to the fact that the minimal distortion condition is covariant, while the Gamma-freezing condition is not.

B. Evolution of the hydrodynamics equations

An important feature of the `Whisky` code is the implementation of a *conservative formulation* of the hydrodynamics equations [40–42], in which the set of Eqs. (2) is written in a hyperbolic, first-order and flux-conservative form of the type

$$\partial_t \mathbf{q} + \partial_i \mathbf{f}^{(i)}(\mathbf{q}) = \mathbf{s}(\mathbf{q}), \tag{7}$$

where $\mathbf{f}^{(i)}(\mathbf{q})$ and $\mathbf{s}(\mathbf{q})$ are the flux-vectors and source terms, respectively [43]. Note that the right-hand side of Eq. (7), i.e., the source vector $\mathbf{s}(\mathbf{q})$, depends only on the metric, and its first derivatives, and on the stress-energy tensor. Furthermore, while the system (7) is not strictly hyperbolic, strong hyperbolicity is recovered in a flat spacetime, where $\mathbf{s}(\mathbf{q}) = 0$.

Additional details of the formulation we use for the hydrodynamics equations can be found in [28]. We stress that an important feature of this formulation is that it has allowed to extend to a general relativistic context the powerful numerical methods developed in classical hydrodynamics, in particular, high-resolution shock-capturing schemes based on linearized Riemann solvers (see [43] for a extensive discussion of this). Such schemes are essential for a correct representation of shocks, whose presence is expected in several astrophysical scenarios.

III. INITIAL DATA FOR MIXED BINARIES

A. A spectral approach for mixed binaries

The initial data for a binary system composed of a black hole and of a relativistic star of comparable masses have been computed with a modified version of the spectral solver used in Ref. [44] for the solution of the initial-data problem in a binary system of two black holes modeled as punctures [45]. While we refer the interested reader to [44] for the details of the solver, we here concentrate on the modifications needed in order to include matter sources in the initial slice of the spacetime.

In a vacuum spacetime describing two black holes with zero momenta, the only nontrivial equation is the Hamiltonian constraint, which can be written as

$$\tilde{\nabla}^2 \psi - \frac{1}{8}\psi \tilde{R} - \frac{1}{8}\psi^5 K^2 + \frac{1}{8}\psi^5 K_{ij} K^{ij} = 0. \tag{8}$$

where $\tilde{\nabla}^2$ and $\tilde{R}$ are the Laplace operator and the Ricci scalar connected to the conformal metric, respectively. If a nonvacuum configuration is considered, as it is necessary for mixed binary systems, Eq. (8) needs to be extended to

$$\tilde{\nabla}^2 \psi - \tfrac{1}{8}\psi \tilde{R} - \tfrac{1}{8}\psi^5 K^2 + \tfrac{1}{8}\psi^5 K_{ij} K^{ij} = -2\pi\psi^5 e_{\mathrm{ADM}}, \tag{9}$$

where

$$e_{\mathrm{ADM}} = n^\mu n^\nu T_{\mu\nu} = W^2(\rho(1+\epsilon) + p) - p \tag{10}$$

is the energy density measured by an observer moving orthogonally to the spacelike hypersurface with normal unit vector $\boldsymbol{n}$ and W the Lorentz factor.

It can be shown that it is not possible to solve Eq. (9) directly using e_{ADM} since this does not produce a solution in general [46]. Rather, it is necessary to adopt a new quantity $\bar{e}$ related to e_{ADM} as

$$\bar{e} = \psi^n e_{\mathrm{ADM}}, \tag{11}$$

where the exponent n is arbitrary but for the condition $n > 5$ (see Ref. [46] for the different possible choices). We have used $n = 8$ so that Eq. (9) becomes

$$\tilde{\nabla}^2 \psi - \tfrac{1}{8}\psi \tilde{R} - \tfrac{1}{8}\psi^5 K^2 + \tfrac{1}{8}\psi^5 K_{ij} K^{ij} = -2\pi\psi^{-3}\bar{e}. \tag{12}$$

The quantity $\bar{e}$ is first computed using Eq. (11) from the conformal factor ψ and from the initial guess for the fluid quantities (p, ρ and ϵ), and then held fixed while solving Eq. (12). From $\bar{e}$ and the new solution for ψ, the new e_{ADM} can be obtained again through Eq. (11) and, as a result, also the new values for the fluid quantities using Eq. (10) and the polytropic EOS with $\Gamma = 2$. As initial guess we used the solution for a spherically symmetric star in equilibrium.

An accurate solution to Eq. (12) can be found using spectral methods and a set of coordinates (A, B, ϕ) which are suitably adapted to the geometry of the problem and which are related to the Cartesian ones through the transformation

$$x = \frac{2B(A^2+1)}{(A^2-1)(1+B^2)} b, \tag{13}$$

$$y = -\frac{2A(1-B^2)}{(A^2-1)(1+B^2)} b\cos\phi, \tag{14}$$

$$z = \frac{2A(1-B^2)}{(1-A^2)(1+B^2)} b\sin\phi, \tag{15}$$

where b is half of the separation between the two singularities, ϕ is the standard azimuthal coordinate in a spherical polar coordinate system, and the coordinates A and B

are restricted to be

$$A \in [0, 1], \qquad B \in [-1, 1], \qquad \phi \in [0, 2\pi). \tag{16}$$

Figure 1 provides a schematic picture of the coordinate setup and the location of the star and of the black hole in both spaces of coordinates.

Following the puncture approach, we decompose ψ into a part which is a known solution to Eq. (9) and contains the contribution of the single black hole, and an unknown part u

$$\psi = 1 + \frac{m}{2r} + u. \tag{17}$$

As a result, Eq. (9) reduces to an equation of the type

$$f(u) = \tilde{\nabla}^2 u = 0. \tag{18}$$

Clearly, Eq. (18) does not have any singular behavior and can be computed very accurately as discussed in Ref. [44]. Note that in the case of a vacuum spacetime the momentum constraint equation can be solved analytically and thus the simplifying assumption of zero momenta can be dropped. When matter sources are present, on the other hand, this is no longer possible. Because of the added complications coming from this, hereafter we will restrict ourselves to considering the simplest case in which both the black hole and the compact star to have zero momenta, i.e., $j^i = 0$. As a result Eq. (12) reads

$$\tilde{\nabla}^2 \psi = -2\pi \psi^{-3} \bar{e}. \tag{19}$$

The use of the coordinate system (13) has also the important advantage that it compactifies the spatial domain and thus allows for an accurate measurement of the ADM mass on the spacelike slice

$$M_{\rm ADM} = \frac{1}{16\pi} \int (\alpha \sqrt{\gamma} \gamma^{ij} \gamma^{kl} (\gamma_{ik,j} - \gamma_{ij,k}))_{,l} \mathrm{d}^3_x \tag{20}$$

$$= \frac{1}{16\pi} \oint_\infty \alpha \sqrt{\gamma} \gamma^{ij} \gamma^{kl} (\gamma_{ik,j} - \gamma_{ij,k}) \mathrm{d}S_l. \tag{21}$$

where the second expression converts the volume integral to a surface one. This latter expression is also evaluated on the grid used for the time evolution over the largest cuboidal surface that can be fitted on the finite-size computational domain covered by the Cartesian coordinates. Clearly, this represents an approximation to the actual ADM mass and the overall error can be estimated by comparing the values of $M_{\rm ADM}$ as computed initially on the compactified, spectral grid with the one estimated on the Cartesian grid. This fractional error is as shown as a function of the linear grid size in Fig. 2, where the two curves show the error whether or not the lapse function in Eq. (21) is set to be one as in an asymptotically flat spacetime. For each choice of grid size, this error will determine the size of an ''error-bar'' indicating the smallest error for the measurement of the ADM mass for the typical grid resolutions used in our simulations; (cf. the error-bar in Fig. 9).

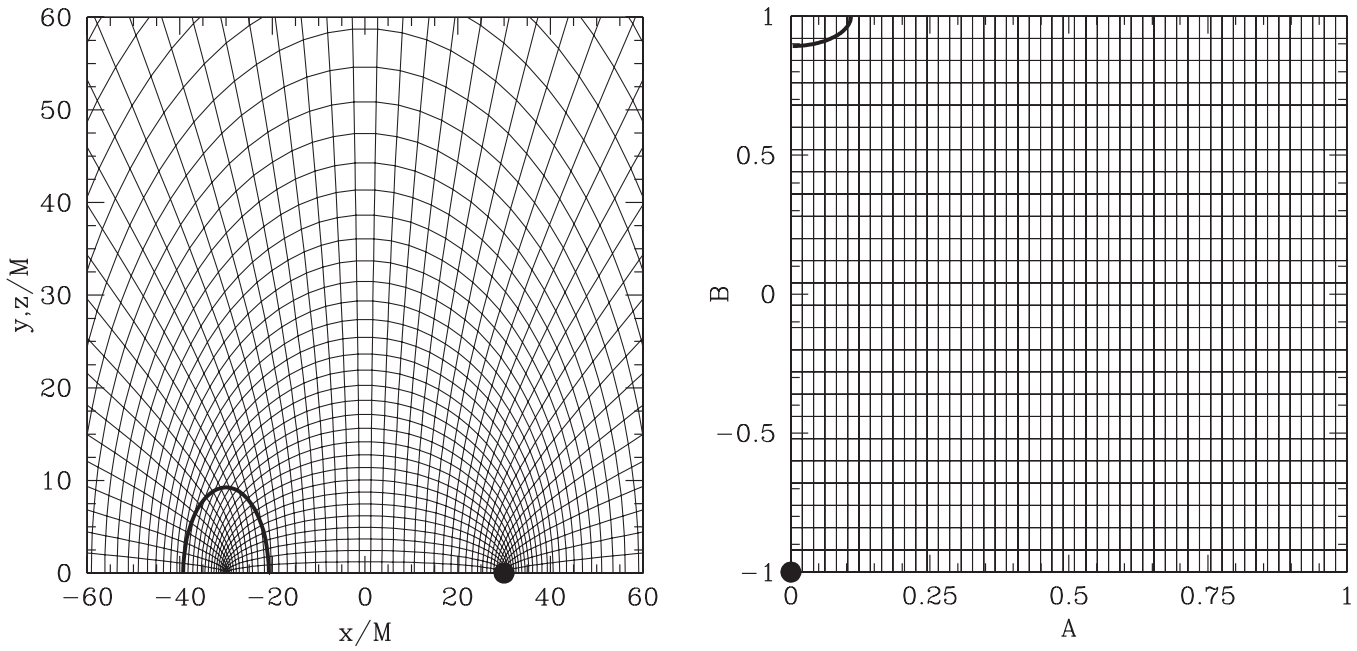

FIG. 1. *Left panel:* Coordinate lines of A and B on the Cartesian grid. The arrow denotes the location of the singularity ($b = 30$) and the sector is a sketch of the neutron star. *Right panel:* coordinate lines of A and B on their grid. The arrow denotes the location of the singularity and the sector is a sketch of the neutron star.

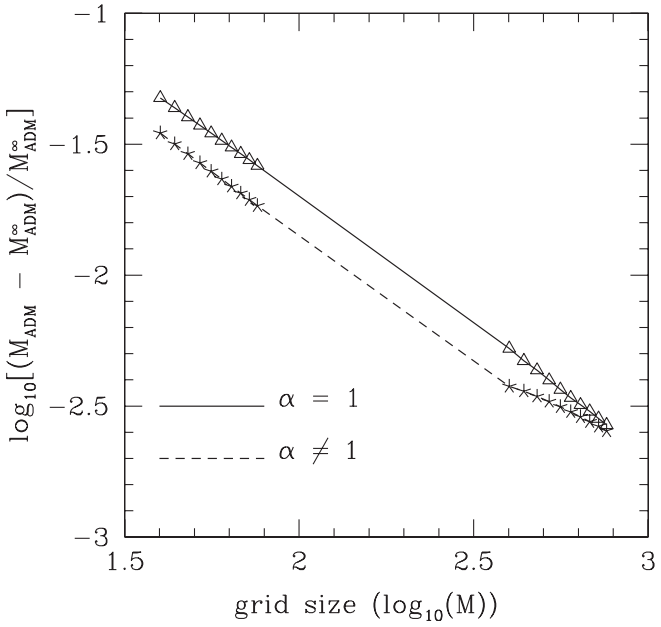

FIG. 2. Fractional error in the evaluation of the ADM mass resulting from a finite-size computational domain. The two curves show the error in the different cases in which the lapse function in Eq. (21) is set to be one or not.

Once the solution to Eq. (12) is found with the desired accuracy on the spectral grid, it is then evaluated on a Cartesian grid and used as initial data for the subsequent evolution. The evaluation on the Cartesian grid can be done by either using the same set of spectral coefficients used for the spectral solution (see discussion in Ref. [44]) or by simply performing a polynomial interpolation of the desired variables from the spectral grid onto the Cartesian one. The first approach has the advantage of being much more accurate but is also extremely costly from a computational standpoint; furthermore, as the accuracy during the evolution is dominated by the truncation error and not by the error coming from the initial data, we routinely import the spectral solution onto the Cartesian grid by means of a simple and comparatively inexpensive third-order polynomial interpolation.

It is worth noting that even in the case of compact objects of comparable mass, a much higher resolution is needed in the vicinity of the black hole. This is due partly to the fact that the spacetime curvature varies there more rapidly and partly to the need of having a sufficient resolution for the excision technique to operate satisfactorily. Because the use of a high-resolution, uniform grid would be computationally too expensive, we use a Berger-Oliger type, box-in-box, fixed mesh-refinement [47] as provided by the `Carpet` code [48]. The resulting setup of the computational domain is sketched in Fig. 3. Note that we use a total of six levels of mesh refinement, three of which refine the region around the black hole. Note also that the use of reflection symmetry across the x-y and the x-z planes, gridpoints are needed only at positive y and positive z coordinates.

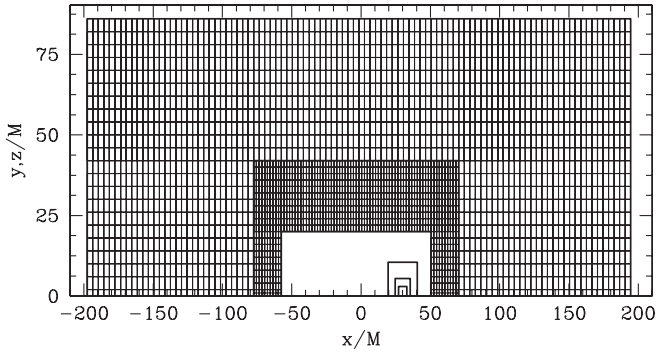

FIG. 3. Computational setup of the mixed binary problem discussed here. Shown are the borders of the six mesh-refinement levels (The actual resolution is higher than sketched here). Because of the use of reflection symmetry at the x-y and the x-z plane, we only have to use grid points at positive y and positive z coordinates.

Hereafter we will concentrate on two different grid resolutions which will refer to as ''low'' and ''high-resolution'', respectively. In the first one we set the coarsest and finest grid spacings to be $\Delta_{\rm coarse} = 4.0M$ and $\Delta_{\rm fine} = 0.125M$, respectively, ($\Delta_{\rm coarse} \approx 0.69M_{\rm ADM}$ and $\Delta_{\rm fine} \approx 0.02M_{\rm ADM}$). For the high-resolution grid, on the other hand, we choose $\Delta_{\rm coarse} = 2.0M$ and $\Delta_{\rm fine} = 0.0625M$.

B. Initial data testing

The use of a spectral method for the calculation of the initial data has the considerable advantage of providing an exponential convergence rate when the solution is of class $\mathcal{C}^{\infty}$. This important property is however lost when the solution comprises matter source terms like in our case since these are of class $\mathcal{C}^0$, so that ψ is of class $\mathcal{C}^2$. In this case the convergence rate is third-order in the number of coefficients $N_{\rm S}$ used in the spectral expansion. We have tested and verified this scaling behavior by setting the energy density on the right-hand side of Eq. (19) to be the energy density of a spherical star in equilibrium. Because the latter can be calculated to great accuracy as a solution of an ordinary differential equation, all of the truncation error is the one related to the spectral solver and we have found it to be the expected third-order.

This is summarized in Fig. 4 which shows the 2-norm of the Hamiltonian constraint as a function of the grid-spacing Δx and of the number of for the initial data. In particular, different lines refer to solutions computed with the spectral method and with a number of spectral coefficients ranging from $N_{\rm S} = 30$ to $N_{\rm S} = 480$. The initial data is then imported onto a Cartesian grid having a spacing ranging from $\Delta = 0.5M$ to $\Delta = 0.125M$ and the Hamiltonian constraint (which we recall involves second-order spatial derivatives) is then computed using a fourth-order accurate finite-difference stencil. Clearly,

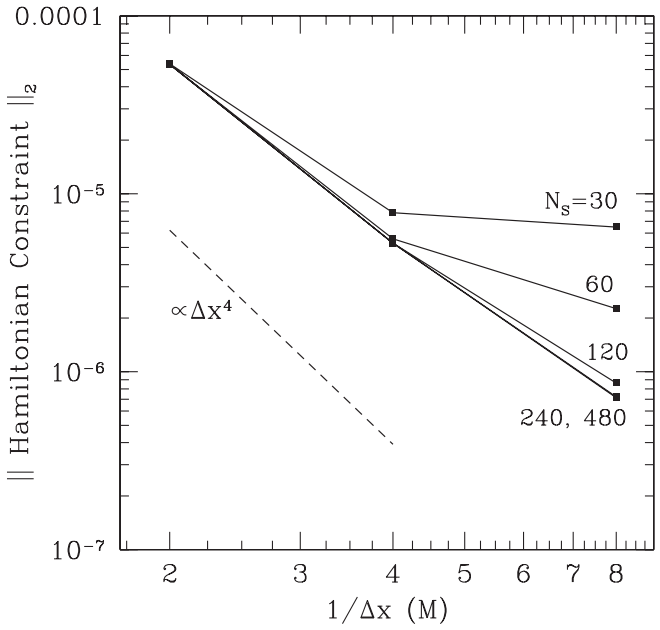

FIG. 4. 2-Norm of the Hamiltonian constraint along the x-axis for different resolutions of the spectral and the Cartesian grid. The dashed line corresponds to a fourth-order convergence rate and is offered as a comparison.

for small Cartesian resolution (i.e., $\Delta = 0.5M$) the finite-differencing error is the largest for any number of the spectral coefficients. On the other hand, as the Cartesian discretization decreases, the truncation error resulting from the spectral solution becomes comparable with the finite-difference one. As a result, more and more spectral coefficients are needed to reach the desired fourth-order convergence and whose representative slope is indicated with a dashed line.

Figure 4 also shows that only when a sufficient number of spectral coefficient is used (i.e., $N_S \gtrsim 240$) is the total truncation error dominated by the finite-differencing and that the latter is not exactly of fourth-order but somewhat smaller (i.e., ≈ 3.3). The reason for this is that the initial-data solution shows very small oscillations on the spectral grid because of the nondifferentiability of the fluid variables at the surface of the star. Although spurious, these oscillations in the solutions are well-resolved on the spectral grid but cannot be satisfactorily reproduced onto the Cartesian grid, despite the resolution being largely increased in the vicinity of the two compact objects. As a result, the fourth-order convergence rate is lost in these regions and it is consequently spoiled overall, bringing it to the measured value of 3.3.

To test the accuracy of the initial-data solver we have therefore considered binary configurations not suffering from this problem (e.g. with vacuum solutions of punctures) and recovered in those cases the expected fourth-order convergence. We also note that while a degraded convergence rate in the initial data is annoying, it is rather inevitable, at least with the present choice of the domain decomposition for the spectral grid and with the presence of matter terms which are not of class $\mathcal{C}^\infty$. As a result, and at least in principle, a solution to this problem could be obtained by using multiple domains one of which would cover the matter source entirely and whose edges would coincide with the stellar surface. In practice, however, any additional effort in reducing the error in the initial data would probably not translate into a direct advantage for the evolution, since the truncation error coming from the finite-difference operators always represents the largest contribution to the error. In view of this, we have not pursued this effort further.

IV. RESULTS

A. Improved gauges and excision

Two important changes with respect to the evolutions discussed in Refs. [28,49] have been introduced in this work and have turned out to be essential in achieving the long-term stability needed to perform the head-on collision.

The first of these changes is the introduction of an artificial dissipation of the Kreiss-Oliger type [50] on the right-hand-sides of the evolution equations for the space-time variables and the gauge quantities. More specifically, for any time-evolved quantity q, the right-hand-side is modified with the introduction of a term of the type

$$\mathcal{L}_{\rm diss}(q) = -\varepsilon \partial_x^4 q, \tag{22}$$

where $\varepsilon = \varepsilon(x, \Delta x)$ is the dissipation coefficient, it is not necessarily constant in space and it decreases more rapidly than the truncation error associated to $\mathcal{L}$, i.e. $\varepsilon \propto \Delta x^3$.

Using a second-order finite-difference representation of the fourth-order partial derivative, Eq. (22) takes the form

$$\mathrm{L}_{\rm diss}(q_i) = -\frac{\varepsilon}{16}\frac{(q_{i-2} - 4q_{i-1} + 6q_i - 4q_{i+1} + q_{i+2})}{\Delta x^4} + \mathcal{O}(\Delta x^2). \tag{23}$$

While the additional dissipative term is applied throughout the grid, its magnitude will be different according to whether a gridpoint is inside or outside the apparent horizon which, within the `Cactus` code, is obtained using the fast finder of Thornburg [51,52]. More specifically, for all gridpoints outside the apparent horizon we set $\varepsilon(x) = \varepsilon^{\rm out} \ll 1$ and a small amount of dissipation will here serve to damp the small oscillations produced at the mesh-refinement boundaries and which can potentially lead to instability (see [48] for a complete discussion). For all gridpoints inside the apparent horizon, on the other hand, we set $\varepsilon(x) = \varepsilon^{\rm in} \gg \varepsilon^{\rm out}$ and the transition from the two values can be specified through a parametrized slope. The latter does not seem to influence significantly the quality of the evolution and most of the time a steep, linear slope is sufficient.

The optimal values of $\varepsilon^{\rm out}$ and $\varepsilon^{\rm in}$ depend on the specific problem at hand. Clearly, excessively small values will not produce any benefit while values that are too large will lead to numerical instabilities. For the results presented here we have found that a long-term stability was obtained for $\varepsilon^{\rm out} = 0.01$ and $\varepsilon^{\rm in} = 0.1$

The second important change introduced is related to improved gauge conditions that minimize the motion of the black hole on the grid and which, in the absence of an algorithm to handle a moving excised region on the numerical grid, would inevitably lead to rapid crash of the code. An obvious solution to this problem is to allow for the motion of the excised region, which, in turn, requires a proper handling of the regions of the grid that need no longer to be excised, but rather to be populated with relevant data (see e.g. [53–55]). While this is technically possible, it is not yet implemented in our code. Alternatively, it is possible to increase progressively the size of the excision region while making sure that all points inside this region stay inside. Clearly, this is a solution which has only a limited validity and works well only for very small mass ratios or up until the excised region has grown to be comparable with the size of the apparent horizon. A third possibility, and which has proven to be successful in our implementation, is to minimize the black hole movement by letting the whole grid move towards it. In practice, this entails a suitable use of the gauge conditions for the shift based on the knowledge of the position of the apparent horizon. This idea is not new (see, for instance, Ref. [56]) and amounts to correcting the Gamma-driver shift condition (6) with an additional term which reflects a coordinate acceleration towards the black hole. This is most conveniently done by modeling the changes as those experienced by a damped harmonic oscillator [57].

More specifically, assuming x_m to be the coordinate position of the apparent horizon and x_d the desired one so that $x_h \equiv x_m - x_d$ measures the deviation from the optimal position, the contribution to the shift evolution coming from this correction can be calculated using the damped harmonic-oscillator equation

$$T^2 \ddot{x}_h + 2Td\dot{x}_h + x_h = 0 \tag{24}$$

where T is the frequency of the harmonic oscillation and d/T the decay time for the oscillation. In practice this leads to an acceleration

$$\ddot{x}_h = -\frac{1}{T^2}(2Td\dot{x}_h + x_h), \tag{25}$$

which is added to the right-hand-side of the evolution equation for the shift vector (6).

The constants T and d need to be chosen accurately in order to obtain the desired behavior and our experience is that excessively small values for T or excessively large values for d can lead to instabilities. Similarly, a too large value for T reduces the effect of this correction, while too small a value for d can lead to undesired oscillations in the shift. Overall, we have found that values of $T = 10$ and $d = 1$ work best in our particular case. Using this correction, the position of the apparent horizon can be held fixed on the numerical grid, which increases the lifetime of the simulations from $\approx 230M$ to $\approx 1700M$.

B. Dynamics of the collision

Although our approach is rather generic and could allow for a very large range of mass ratios and separations between the two compact objects, hereafter we will concentrate on a prototypical mixed binary system consisting of a initial guess for the neutron star with a gravitational mass of $0.86M$, proper radius $R = 10.49M$ (i.e., $M/R = 0.08$), and a Schwarzschild black hole with a mass of $5M$. The coordinate separation is $60M$ [i.e., $b = 30$ in Eq. (13)]. The initial velocities are taken to be zero and the initial data conformally flat and time-symmetric. The ADM mass, as measured on the compactified, spectral grid, is $5.78M$.

As one would expect, the combined perturbations coming from the truncation error (cf., results from the evolution of isolated stars [28]) and from the black hole's tidal field [58], induce oscillations dominated by the fundamental mode. These oscillations appear to be harmonic up until the gravitational influence of the black hole becomes apparent and therefore changes the nature of the oscillating mode. In our simulation, the star is not in equilibrium. This perturbation also produces oscillations like the ones introduced by the truncation error, but with much bigger amplitude. This is illustrated in Fig. 5 where we show with a solid the time evolution of the maximum rest-mass density (which coincides with the rest-mass density at the center of the star). Indicated with a dashed line is also a trigonometric function at the frequency of the fundamental (f) mode of the unperturbed star which was measured to be $\approx$ 1.28 kHz in a separate simulation. Note also that the star oscillates for a bit longer than a full period before it is tidally disrupted and fully accreted onto the black hole, which occurs at $\simeq 350M$. The central density rises considerably during the accretion process with a net increase of a factor of about 2.5. For stars that are in eccentric orbits with very close periastrons and that are sufficiently close to the stability threshold, the monotonic increase in central density produced by the black hole's tidal field could lead to either phase transition [59] or to the collapse to a black hole. In both cases, which we plan to investigate in subsequent work, a copious emission of gravitational waves would be produced.

A self-explanatory description of the matter evolution is presented in Fig. 6 which shows consecutive snapshots of the stellar motion towards the black hole. Different panels are separated in time of about $50M \simeq 0.25$ ms and refer to logarithmically spaced isocontours of the rest-mass density in the (x, y) plane. Also shown with a dashed line is the

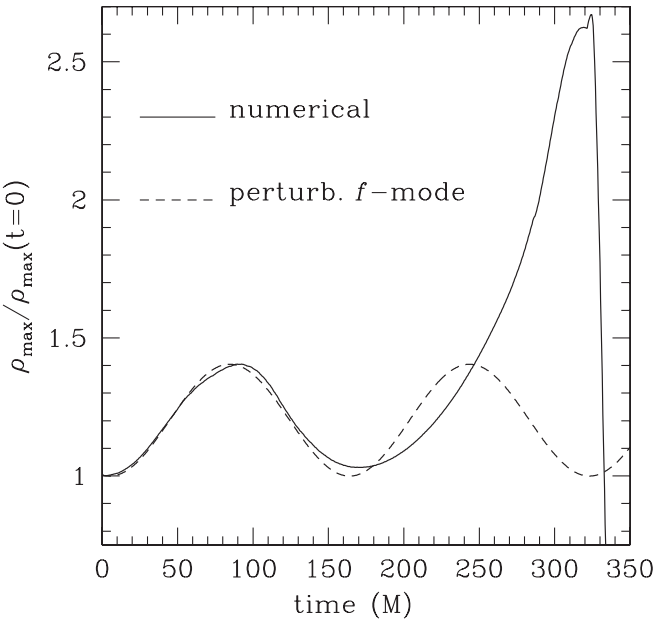

FIG. 5. Shown is the maximal rest-mass density ρ over time (solid line) and as comparison a trigonometric function with the frequency of the fundamental mode of the unperturbed star of which is ≈ 1.28 kHz.

coordinate shape of the apparent horizon, while the filled area in its interior refers to the excised region.

Note that the stellar model is initially spherically symmetric and that in about a sonic crossing time it starts to move towards the black hole. As it does so, it also experiences an increasingly strong tidal field which leads to a flattening of the star which then assumes the typical olive-shaped profile. The accretion process takes place between $t \simeq 280M$ and $t \simeq 340M$, so that by $t \simeq 350M$ essentially no matter is left outside the apparent horizon. Note also that the evolution proceeds well after this time and indeed an accurate evolution with moderate growth of the constraint violation is possible up to a time $t \sim 1700M$, i.e., approximately $1300M$ past when the last stellar fluid-element has been accreted onto the black hole (see also Figs. 9 and 11) [60]. We consider this a significant achievement in numerical simulations involving nonvacuum and nonstationary black hole spacetimes. To underline how this represents remarkable improvement with respect to the present state-of-the-art calculations, we note that in our recent investigations of the collapse of a rotating star to a Kerr black hole [28], we were able to prolong the evolution of $\sim 30M$ past the appearance of the apparent horizon and the introduction of an excised region and only $\sim 10M$ after the star was fully accreted onto the excised region.

Figure 7 shows the corresponding evolution across the (x, y) plane of a representative metric function, i.e., g_{xx}, during the collision and accretion. The solution shown refers to the coarsest grid only and the circle across the $y = 0$ axis shows the position of the apparent horizon. Also in this case the evolution presented in the different panels is self-explanatory and worth underlining is only the regularity of the solution during the accretion process and the rapid recovery of the solution for an isolated black hole after $t \simeq 300M$.

Figure 8 offers a closer look of the final stages of the collision starting from $t = 265M$ and with a progression of $10M$ (time progresses from the upper-left corner to the lower-right one). Note the progressive flattening of the

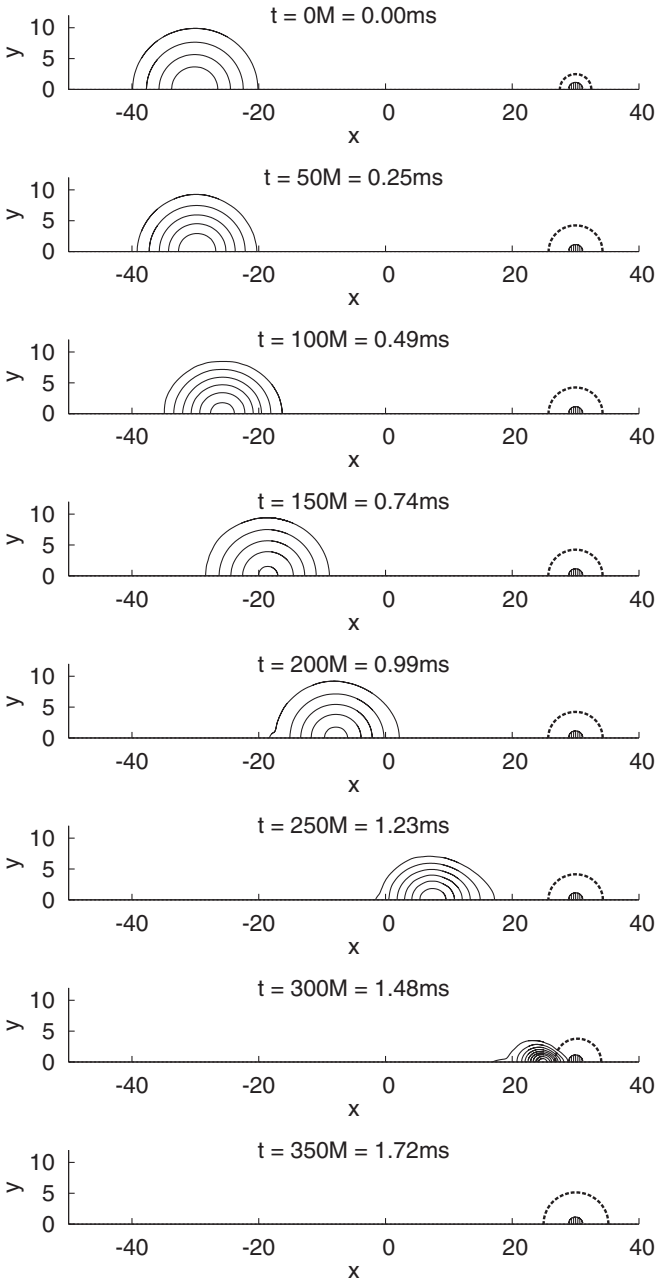

FIG. 6. Isocontours of the rest-mass density and of the apparent horizon surface (dashed line) in the (x, y) plane; the area shown as filled refers to the excised region of the computational domain. The different panels refer to times from $0M$ to $350M$ in steps of $50M \simeq 0.25$ ms.

neutron star produced by the tidal field and the long ''tail'' resulting from the strong rarefaction and produced by the rapid accretion from $t \simeq 295M$ to $t \simeq 325M$. Note also that the matter dynamics is accurately described well within the apparent horizon (dashed thick line in Fig. 7) and that the motion into the excised region (shaded area in Fig. 7) takes place very smoothly without the appearance of irregularities in the flow. This is the result of self-consistent treatment of the flow across the excision region and which makes full use of the characteristic information [49].

The sequences shown in Figs. 6–8 are also useful to appreciate the effectiveness of the improved gauge conditions. Note, in fact, how the position of the black hole does not change perceptibly despite the binary system has a mass ratio of $\simeq 5.8$. When looked at carefully, the apparent horizon increases its coordinate dimensions during the early stages of the evolution as it does also as a result of the accreted stellar mass. Clearly, the first of these growths is just a coordinate effect resulting from our gauge choice which moves grid points outwards from the apparent horizon and leads to its coordinate growth. Indeed, when looked at in terms of its proper dimensions, the apparent horizon does not show a significant increase during the early stages of the evolution and its growth is essentially confined to the time during which matter is accreting onto it. This is shown in Fig. 9 which presents the time evolution

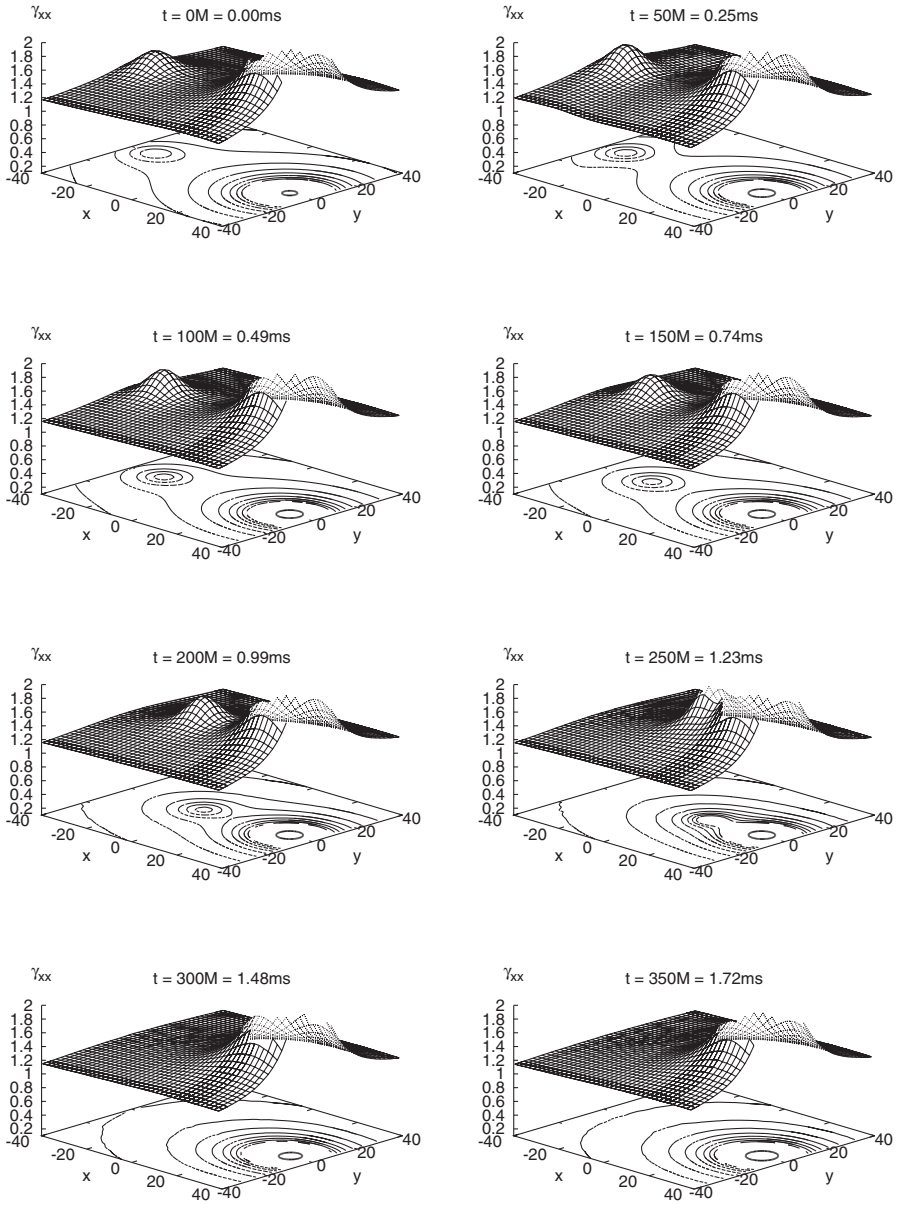

FIG. 7. Time evolution of a representative metric function (i.e., g_{xx}), in its cross-section onto the (x, y) plane, with the circle across the $y = 0$ axis showing the position of the apparent horizon. The different panels refer to times from $0M$ to $350M$ in steps of $50M \simeq 0.25$ ms and we have reported only the solution evaluated on the coarsest grid.

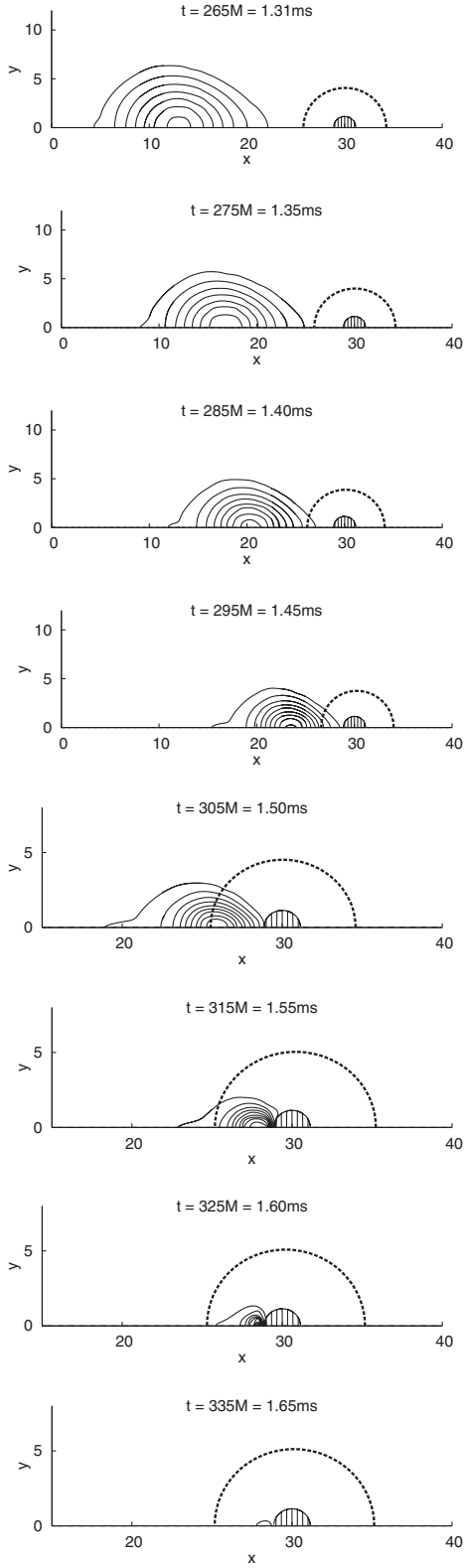

FIG. 8. Isocontours of the rest-mass density and of the apparent horizon surface (dashed line) in the (x, y) plane; the area shown as filled refers to the excised region of the computational domain. The different panels refer to times from $265M$ to $335M$ in steps of $10M$. Note that the scale in the first four frames is different (larger) than the one in the last four frames.

of the horizon mass for both a low and a high-resolution simulation (dashed and continuous curves, respectively) and compares it with the expected ADM mass (i.e., as measured on the Cartesian grid and indicated with a dotted line) and the error bar resulting from the use of a computational domain of finite extent.

A number of comments are needed here. First, it should be noted that the apparent horizon mass is not constant before the merger but shows a small, constant drift to higher masses. This is clearly the result of a large truncation error, especially near the apparent horizon, and is considerably reduced in the high-resolution run. Second, it is apparent that the increase in the horizon mass is essentially limited to the time interval during which the neutron star is accreted onto the black hole, that both measures are compatible with the expected error-bar and that as the resolution is increased the error in the expected mass-growth before merger is also progressively reduced. Finally, note that after the merger the mass of the apparent horizon does not remain constant but rather decreases slightly, so that by the time the simulation is completed, the black hole has lost about 0.7% of its mass. While a mass-loss is in principle expected as a result of the emission of gravitational radiation from the oscillating black hole, in Sec. V we will show that indeed the latter is much smaller and hence the secular mass-loss in the post-merger

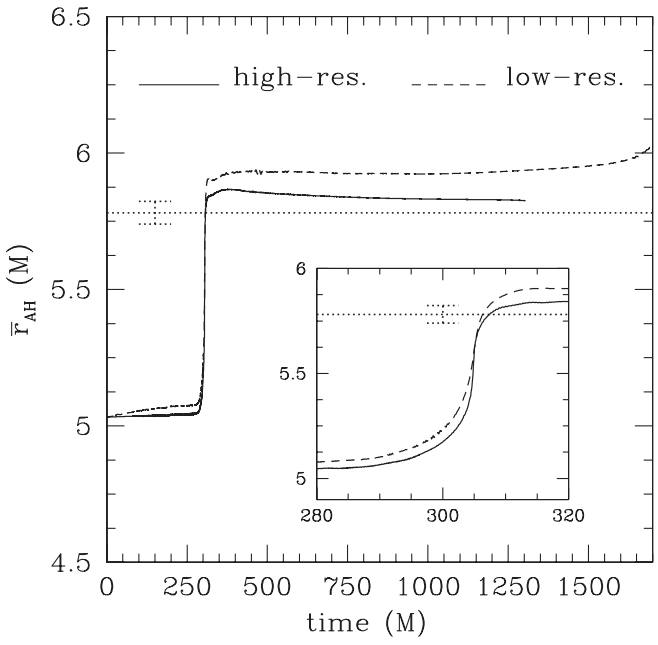

FIG. 9. Time evolution of the mass of the apparent horizon shown for a high-resolution simulation (solid line) and a low-resolution one (dashed line). Indicated with a horizontal dotted line is the expected ADM mass and the error-bar indicates the error introduced by a finite-size domain for the smallest resolution used. The inset shows the evolution around the time of the accretion of the neutron star onto the black hole.

evolution is small and essentially due to the truncation error.

Besides the growth in area, the black hole is also expected to experience quasinormal mode (QNM) oscillations as a response to the collision. We have carefully looked at whether these oscillations are detectable and we show with a solid line in Fig. 10 the time evolution of the ratio between the polar and equatorial proper circumferences soon after the collision has taken place. In order to assess whether this damped oscillation does correspond with the expected QNM we compare this behavior with the one expected from perturbative analyzes which predict the frequency of the $\ell = 2$ fundamental ($n = 0$) QNM to be [61,62]

$$f \simeq 0.374[2\pi(5.14\ \text{kHz})(M_\odot/M)]. \tag{26}$$

or equivalently $f = 2.06$ kHz for a black hole mass of $\simeq 5.86M$ and an expected damping time of 0.32 ms for the same mass. The corresponding QNM behavior is shown as a dashed line in Fig. 10 for the high-resolution simulation. The rather good agreement is an important confirmation that the oscillation detected is not a numerical by-product but embodies important physical information. Perhaps even more impressive than the good matching with the perturbative results is the consideration that the QNM oscillations shown in Fig. 10 have indeed a very small amplitude of less than 2%; the ability of our code to detect it is a confirmation of the overall accuracy achieved but also an indication that high-resolution near the black hole apparent horizon is crucial for a consistent modeling of the black-hole dynamics.

We conclude this section by showing in Fig. 11 a one-dimensional (1D) slice of the Hamiltonian constraint violation along the x-axis at a representative time $t = 100M$. Each panel in the Figure reports two curves at two different resolutions, the solid line referring to a low-resolution grid and the dashed one to a high-resolution grid rescaled by a factor of 4 to highlight the second-order convergence. Furthermore, while the left panel shows the portion of the grid comprising the two compact objects, the right one offers a closer look at the violation in the vicinity of the black hole. A couple of aspects of Fig. 11 are worth highlighting. First, the rapid variation of the constraint violation shown in the Figure is due to the slightly different truncation errors in the regions where two refinement levels overlap and which is magnified when the second spatial derivatives are calculated in the calculation of the Hamiltonian constraint. Second, the rate of convergence is different in different parts of the grid, being somewhat less than second-order over the regions covering the matter sources and which are probably not sufficiently resolved. Finally, the convergence rate is higher in those regions of the domain where the fields do not vary rapidly (we recall that Fig. 11 shows only a small portion of the numerical grid which extends from $x \sim -200M$ to $x \sim 200M$).

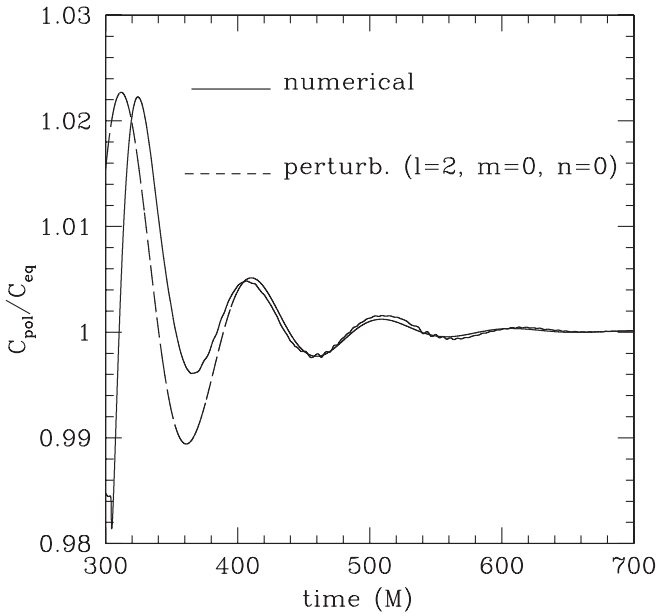

FIG. 10. Time evolution of the ratio between the polar and equatorial proper circumferences of the apparent horizon soon after the collision (solid line). Shown for a comparison with a dashed line is the QNM oscillation of a black hole with mass $\simeq 5.86M$, fundamental $\ell = 2$ frequency of $f \approx 2.06$ kHz and damping time of 0.32 ms.

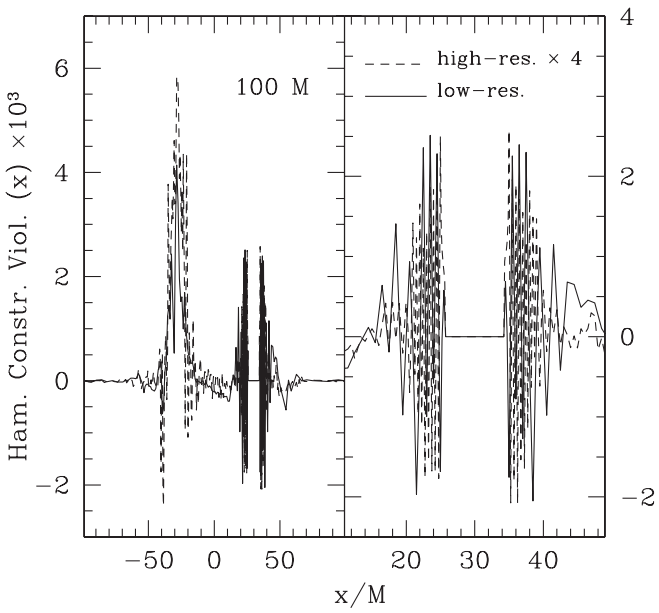

FIG. 11. 1D slice of the Hamiltonian constraint violation along the x-axis at a representative time $t = 100M$. Each panel reports two curves indicating, respectively, the violations computed with a low-resolution grid (solid line) and with a high-resolution one (dashed line) scaled by a factor of 4 for the expected second-order accuracy. While the left panel shows the portion of the grid containing the two compact objects, the right one focuses on the violation around the black hole.

Overall, the evolution of more global quantities, such as the 2-norm of the Hamiltonian constraint violation show that the norm increases by roughly 3 orders of magnitude soon after the simulations start. This simply indicates that the errors in the determination of the initial data are much smaller than the ones introduced by the evolution of these data. At the time of merger (i.e., at $t \approx 300M$), the violation increases rapidly by roughly an order-of-magnitude (and can be locally even larger) as a result of the matter crossing many mesh-refinement boundaries and finally the excision boundary. Once the collision has taken place and all of the matter has been accreted onto the black hole, the constraint violation settles to a constant but somewhat smaller value than the one before the merger since no matter is left in the computational domain and this suppresses the contribution to the violation of the Hamiltonian constraint coming from the matter terms [cf. eq. (2.6) in [28]]. Also, the code maintains second-order convergence up until the errors coming from the excision boundary spoil the convergence and thus increase the truncation error. From shortly after the merger up to $t \approx 1700M$ the violation is roughly constant, until a rapid instability appears which grows exponentially and leads to a code crash. It is still unclear what is the precise source of this instability, although it is apparent that the boundary conditions we use are not constraint-preserving and may be behind the onset of the instability. Work is now in progress to improve the outer boundary conditions making use of the numerous results which have been obtained recently in the literature about this, e.g. Refs. [63–67].

V. GRAVITATIONAL-WAVE EMISSION

Several different methods can be used to extract gravitational waves from a numerical simulation. Here we use a gauge-invariant approach, in which the numerical spacetime is matched to perturbations of a Schwarzschild black hole (see Refs. [68–70]). Because our numerical grid for the evolution does not extent to spacial infinity, we have to measure the gravitational-wave content at a finite distance from the final black hole. In practice we calculate the gauge-invariant metric perturbations $Q_{lm}^{(\mathrm{odd})}$ and $\Psi_{lm}^{(\mathrm{even})}$ [71] as observed on spheres with constant radial coordinate distance from the final black hole. l and m are the indices of the angular decomposition, of which we compute up to $l = 5$ and restrict to m to 0, because modes with $m \neq 0$ are essentially zero due to the axisymmetry of the merger.

Using the odd and even-parity perturbations defined as $Q_{lm}^{\times} \equiv \lambda Q_{lm}^{(\mathrm{odd})}$ and $Q_{lm}^{+} \equiv \lambda \Psi_{lm}^{(\mathrm{even})}$, where $\lambda \equiv \sqrt{2(l+2)!/(l-2)!}$, we calculate the transverse traceless gravitational-wave amplitudes in the two polarizations h_+ and $h_\times$ as

$$h_+ - \mathrm{i}h_\times = \frac{1}{2r}\sum_{l,m}\left(Q_{lm}^{+} - \mathrm{i}\int_{-\infty}^{t} Q_{lm}^{\times}(t')dt'\right){}_{-2}Y^{lm}, \quad (27)$$

where ${}_{-2}Y^{lm}$ is the $s = -2$ spin-weighted spherical harmonic.

The position of such "observers" is arbitrary so long as they are in a region of spacetime which is reasonably close to that of a Schwarzschild spacetime. If the distance to the merging binary is chosen to be too small, the measured perturbations do not contain the same information on the gravitational waves as those in the far zone. One way to test if the position of the observers is chosen far enough away from the final black hole is to extract the perturbations at various different radii. In the far-field region these perturbations have to overlap when plotted in retarded time. In the results presented below, we checked that this is indeed the case.

In Fig. 12 we show h_+ at a (coordinate) distance of $70M$ from the final black hole (waveforms extracted from nearby observers overlap in retarded time confirming that the information is taken in the wave-zone). $h_\times$ is essentially zero because of the symmetries of the head-on merger. The emitted power computed as the total energy lost due to gravitational waves

$$\frac{\mathrm{d}E}{\mathrm{d}t} = \frac{1}{32\pi}\left(\left|\frac{\mathrm{d}Q_{lm}^{+}}{\mathrm{d}t}\right|^2 + |Q_{lm}^{\times}|^2\right), \quad (28)$$

is $E \approx 7.8 \times 10^{-4}(M/M_\odot)$, which corresponds to $\approx 0.013\%$ of the mass of the binary system. This value strongly depends on the time span used for the integration and should be taken only as order-of-magnitude estimate. Overall, this is much smaller than the $\approx 0.1\%$ obtained in the Newtonian simulations mentioned in Sec. I which,

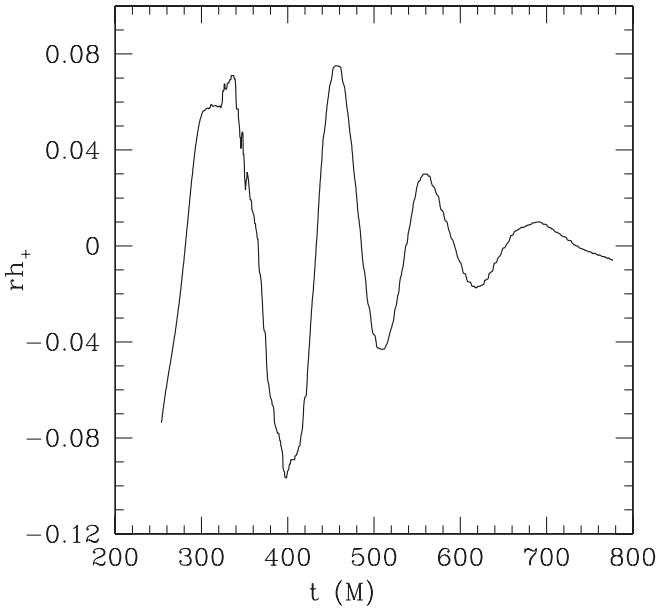

FIG. 12. + component of the gravitational-wave emission from the merging binary system, extracted at a radius of $70M$ from the final black hole. The × component is identically zero.

however, refer to orbiting configurations and are expected to be more efficient emitters.

VI. CONCLUSION

We have discussed the first simulations of a head-on collision of a neutron star and a black hole of comparable mass in full general relativity. This also included the extraction of the gravitational-wave signal produced as well as an order-of-magnitude estimate of the emitted energy.

In this paper, a new approach for obtaining initial data for a mixed binary system has been discussed, which also has been presented in more detail in [72]. This method involves solving the elliptic equation for the Hamiltonian constraint in the York-Lichnerowicz conformal decomposition. The currently used solver uses spectral methods with adapted coordinates on one domain. These initial data are evaluated onto a Cartesian grid structure including fixed mesh refinement. The evolutions are then performed through the full solution of the Einstein equations combined with an accurate solution of the relativistic hydrodynamics equations via high-resolution shock-capturing scheme techniques. Unlike other relativistic studies of such systems, no limitation is set for the mass ratio between the black hole and the neutron star, nor on the position of the black hole, whose apparent horizon is entirely contained within the computational domain. Concentrating on a prototypical binary system with mass ratio ~ 6, we find that although a tidal disruption is evident, the neutron star is accreted promptly and entirely into the black hole.

Two important changes with respect to the evolutions discussed in Refs. [28,49] have been presented, which have been important for long-term stable evolutions. The first of these changes is the use of artificial dissipation, especially to attenuate problems near the excision boundary. The second change is related to special gauge conditions to minimize the motion of the black hole on the numerical grid. This is necessary because we have not yet implemented the possibility of a moving excision region.

We believe that these problems of the excision boundary can be solved in the near future. One reason for this belief is the presence of analytical studies of such boundaries, e.g. based on summation by parts techniques as in [53], which show much better behavior near the excision boundary. Another reason are upcoming codes using multipatch techniques in which it is natural to align excision boundaries to grid boundaries and which show extraordinary stability near the excision region [73]. In addition, evolutions even without excision seem to be possible, provided a very high resolution and dissipation inside the apparent horizon [74]. However, even with the present difficulties encountered in performing long-term stable and accurate calculations of a spacetime including an excised region, we were able to successfully carry out evolutions up to $\sim 1700M$. This is about $\sim 1400M$ after the collision has taken place and provides a sufficient time interval to extract the gravitational-wave signal produced.

We plan to extend the initial data to nonzero momenta in the future. This would allow for orbiting configurations, which should be no particular problem for the evolution techniques used. Other improvements, like the use of a more realistic EOS or the inclusion of magnetic fields are also desirable and will be focus of future work. Finally, it is worth mentioning that the techniques described in this paper can in principle also be applied to the creation of initial data for a binary system of two neutron stars and its evolution. Comparing the differences in the dynamics of the merger of black-hole binaries, mixed binaries and neutron-star binaries, and, in particular, the different efficiencies in the gravitational-wave emission, would also be very interesting and the subject of future work.

ACKNOWLEDGMENTS

F. Löffler is supported by the European Gravitational Observatory (EGO). Support to this research comes also through the SFB-TR7 ''Gravitationswellenastronomie'' of the DFG.

[1] K. Belczynski, V. Kalogera, and T. Bulik, Astrophys. J. **572**, 407 (2002).
[2] V. Kalogera, C. Kim, D. R. Lorimer, M. Burgay, N. D'Amico, A. Possenti, R. N. Manchester, A. G. Lyne, B. C. Joshi, M. A. McLaughlin *et al.*, Astrophys. J. Lett. **601**, L179 (2004).
[3] H. Bethe and G. Brown, Astrophys. J. **506**, 780 (1998).
[4] M. Bejger, D. Gondek-Rosińska, E. Gourgoulhon, P. Haensel, K. Taniguchi, and J. L. Zdunik, Astron. Astrophys. **431**, 297 (2005).
[5] M. Vallisneri, Phys. Rev. Lett. **84**, 3519 (2000).
[6] R. Narayan, B. Paczynski, and T. Piran, Astrophys. J. **395**, L83 (1992).
[7] D. B. Fox, D. A. Frail, P. A. Price, S. R. Kulkarni, E. Berger, T. Piran, A. M. Soderberg, S. B. Cenko, P. B. Cameron, A. Gal-Yam *et al.*, Nature (London) **437**, 845 (2005).
[8] C. Kouveliotou, C. A. Meegan, G. J. Fishman, N. P. Bhat, M. S. Briggs, T. M. Koshut, W. S. Paciesas, and G. N. Pendleton, Astrophys. J. **413**, L101 (1993).
[9] S. F. Portegies Zwart, Astrophys. J. Lett. **503**, L53 (1998).

[10] W. H. Lee and W. Kluzniak, Mon. Not. R. Astron. Soc. **308**, 780 (1999).
[11] W. H. Lee and W. Kluzniak, Astrophys. J. **526**, 178 (1999).
[12] M. C. Miller, Astrophys. J. **626**, L41 (2005).
[13] M. Campanelli, C. O. Lousto, and Y. Zlochower, Phys. Rev. D **73**, 061501 (2006).
[14] P. Diener, F. Herrmann, D. Pollney, E. Schnetter, E. Seidel, R. Takahashi, J. Thornburg, and J. Ventrella, Phys. Rev. Lett. **96**, 121101 (2006).
[15] J. G. Baker, J. Centrella, D.-I. Choi, M. Koppitz, and J. van Meter, Phys. Rev. D **73**, 104002 (2006).
[16] M. Shibata, K. Taniguchi, and K. Uryū, Phys. Rev. D **68**, 084020 (2003).
[17] M. Shibata and K. Taniguchi, Phys. Rev. D **73**, 064027 (2006).
[18] H.-T. Janka, T. Eberl, M. Ruffert, and C. L. Fryer, Astrophys. J. **527**, L39 (1999).
[19] S. Rosswog, Astrophys. J. **634**, 1202 (2005).
[20] T. W. Baumgarte, M. L. Skoge, and S. L. Shapiro, Phys. Rev. D **70**, 064040 (2004).
[21] M. Alcubierre, B. Brügmann, P. Diener, F. S. Guzmán, I. Hawke, S. Hawley, F. Herrmann, M. Koppitz, D. Pollney, E. Seidel *et al.*, Phys. Rev. D **72**, 044004 (2005).
[22] M. Miller, P. Gressman, and W.-M. Suen, Phys. Rev. D **69**, 064026 (2004).
[23] N. T. Bishop, R. Gómez, L. Lehner, M. Maharaj, and J. Winicour, Phys. Rev. D **72**, 024002 (2005).
[24] J. A. Faber, T. W. Baumgarte, S. L. Shapiro, K. Taniguchi, and F. A. Rasio, Phys. Rev. D **73**, 024012 (2006).
[25] K. Taniguchi, T. W. Baumgarte, J. A. Faber, and S. L. Shapiro, Phys. Rev. D **72**, 044008 (2005).
[26] C. F. Sopuerta, U. Sperhake, and P. Laguna, (unpublished).
[27] L. Baiotti, I. Hawke, P. Montero, and L. Rezzolla, in *Computational Astrophysics in Italy: Methods and Tools*, edited by R. Capuzzo-Dolcetta (Mem. Soc. Astron. It. Suppl., Trieste, 2003), vol. 1, p. 327.
[28] L. Baiotti, I. Hawke, P. J. Montero, F. Löffler, L. Rezzolla, N. Stergioulas, J. A. Font, and E. Seidel, Phys. Rev. D **71**, 024035 (2005).
[29] M. Alcubierre, B. Brügmann, T. Dramlitsch, J. A. Font, P. Papadopoulos, E. Seidel, N. Stergioulas, and R. Takahashi, Phys. Rev. D **62**, 044034 (2000).
[30] R. Arnowitt, S. Deser, and C. W. Misner, in *Gravitation: An Introduction to Current Research*, edited by L. Witten (John Wiley, New York, 1962), pp. 227–265.
[31] T. Nakamura, K. Oohara, and Y. Kojima, Prog. Theor. Phys. Suppl. **90**, 1 (1987).
[32] M. Shibata and T. Nakamura, Phys. Rev. D **52**, 5428 (1995).
[33] M. Alcubierre, B. Brügmann, P. Diener, M. Koppitz, D. Pollney, E. Seidel, and R. Takahashi, Phys. Rev. D **67**, 084023 (2003).
[34] C. Bona, T. Ledvinka, C. Palenzuela, and M. Zacek, Phys. Rev. D **69**, 064036 (2004).
[35] G. Nagy, O. E. Ortiz, and O. A. Reula, Phys. Rev. D **70**, 044012 (2004).
[36] M. Alcubierre, B. Brügmann, D. Pollney, E. Seidel, and R. Takahashi, Phys. Rev. D **64**, 061501(R) (2001).
[37] C. Bona, J. Massó, E. Seidel, and J. Stela, Phys. Rev. Lett. **75**, 600 (1995).
[38] M. Alcubierre and J. Massó, Phys. Rev. D **57**, R4511 (1998).
[39] L. Smarr and J. W. York, Phys. Rev. D **17**, 2529 (1978).
[40] J. M. Martí, J. M. Ibáñez, and J. M. Miralles, Phys. Rev. D **43**, 3794 (1991).
[41] F. Banyuls, J. A. Font, J. M. Ibáñez, J. M. Martí, and J. A. Miralles, Astrophys. J. **476**, 221 (1997).
[42] J. Ibáñez, M. Aloy, J. Font, J. Martí, J. Miralles, and J. Pons, in *Godunov Methods: Theory and Applications*, edited by E. Toro (Kluwer Academic/Plenum Publishers, New York, 2001).
[43] J. A. Font, Living Rev. Relativity **6**, 4 (2003), http://www.livingreviews.org/lrr-2003-4.
[44] M. Ansorg, B. Brügmann, and W. Tichy, Phys. Rev. D **70**, 064011 (2004).
[45] S. Brandt, R. Correll, R. Gómez, M. F. Huq, P. Laguna, L. Lehner, P. Marronetti, R. A. Matzner, D. Neilsen, J. Pullin *et al.*, Phys. Rev. Lett. **85**, 5496 (2000).
[46] J. W. York, in *Sources of Gravitational Radiation*, edited by L. L. Smarr (Cambridge University Press, Cambridge, UK, 1979), ISBN 0-521-22778-X, pp. 83–126.
[47] M. J. Berger, Ph.D. thesis, Stanford University, 1982.
[48] E. Schnetter, S. H. Hawley, and I. Hawke, Classical Quantum Gravity **21**, 1465 (2004).
[49] I. Hawke, F. Löffler, and A. Nerozzi, Phys. Rev. D **71**, 104006 (2005).
[50] H.-O. Kreiss and J. Oliger, *Methods for the Approximate Solution of Time Dependent Problems* 10 (World Meteorological Organization, International Council of Scienitfic Unions, 1973).
[51] J. Thornburg, Phys. Rev. D **54**, 4899 (1996).
[52] J. Thornburg, Classical Quantum Gravity **21**, 743 (2004).
[53] G. Calabrese and D. Neilsen, Phys. Rev. D **69**, 044020 (2004).
[54] F. Pretorius, Classical Quantum Gravity **22**, 425 (2005).
[55] U. Sperhake, B. Kelly, P. Laguna, K. L. Smith, and E. Schnetter, Phys. Rev. D **71**, 124042 (2005).
[56] P. Anninos, G. Daues, J. Massó, E. Seidel, and W.-M. Suen, Phys. Rev. D **51**, 5562 (1995).
[57] B. Brügmann, W. Tichy, and N. Jansen, Phys. Rev. Lett. **92**, 211101 (2004).
[58] Indeed, we have verified that the tidal field is the largest source of perturbation. In particular, we have performed a number of simulations with the same spatial resolution but having different initial separations $2d$. If the oscillations were produced by the truncation error, their amplitude would be almost unchanged for different d; on the contrary we have found that the amplitude scales rather well with $1/d$, which is what one would expect from a perturbation induced by a tidal field.
[59] L.-M. Lin, K. S. Cheng, M.-C. Chu, and W.-M. Suen, Astrophys. J. **639**, 382 (2006).
[60] We recall that strictly speaking the spacetime is not pure vacuum also after the last stellar fluid-element. This is because of the presence of the very tenuous atmosphere introduced to use the high-resolution shock-capturing techniques and which does not influence perceptibly the overall dynamics [27,28].
[61] E. Leaver, Proc. R. Soc. A **402**, 285 (1985).
[62] K. D. Kokkotas and B. G. Schmidt, Living Rev. Relativity **2**, 1999 (1999), http://www.livingreviews.org/lrr-1999-2.

[63] A. M. Abrahams, L. Rezzolla, M. E. Rupright, A. Anderson, P. Anninos, T. W. Baumgarte, N. T. Bishop, S. R. Brandt, J. C. Browne, K. Camarda *et al.*, Phys. Rev. Lett. **80**, 1812 (1998).
[64] L. Rezzolla, A. M. Abrahams, R. A. Matzner, M. E. Rupright, and S. L. Shapiro, Phys. Rev. D **59**, 064001 (1999).
[65] G. Calabrese, J. Pullin, O. Reula, O. Sarbach, and M. Tiglio, Commun. Math. Phys. **240**, 377 (2003).
[66] C. Gundlach and J. M. Martin-Garcia, Phys. Rev. D **70**, 044032 (2004).
[67] B. Szilagyi and J. Winicour, Phys. Rev. D **68**, 041501(R) (2003).
[68] M. E. Rupright, A. M. Abrahams, and L. Rezzolla, Phys. Rev. D **58**, 044005 (1998).
[69] K. Camarda and E. Seidel, Phys. Rev. D **59**, 064019 (1999).
[70] G. Allen, K. Camarda, and E. Seidel (1998).
[71] V. Moncrief, Ann. Phys. (N.Y.) **88**, 323 (1974).
[72] F. Löffler, Ph.D. thesis, Max Planck Institute for Gravitational Physics (Albert Einstein Institute), 2005.
[73] J. Thornburg, Classical Quantum Gravity **21**, 3665 (2004).
[74] L. Baiotti and L. Rezzolla, Phys. Rev. Lett. (unpublished).